Effect of Voltage Variation on the Synthesis and Properties of Electrochemically Exfoliated Graphene from Dry-Cell Battery Waste for Chromium Ions Adsorption

Nenden Fauziah[1*], Rini Febi Nuraeni[1], Fitri Dara[2], Rafiq Arsyad[3,4], Nadiatus Silmi[2], and Veinardi Suendo[5,6]

[1]*Department of Chemistry, Faculty of Mathematics and Natural Sciences, Universitas Garut, Jl. Prof. Aam Hamdani No. 42, Garut 44151, Indonesia*

[2]*Research Center for Environmental and Clean Technologies, National Research and Innovation Agency, KST Samaun Samadikun, Jl. Sangkuriang, Bandung 40135, Indonesia*

[3]*Division of Environmental Materials Science, Graduate School of Environmental Science, Hokkaido University, N10W5 Sapporo 060-0810, Japan*

[4]*Institute for Catalysis, Hokkaido University, Kita, Kita-ku, N21W10 Sapporo 001-0021, Japan*

[5]*Division of Inorganic and Physical Chemistry, Faculty of Mathematics and Natural Sciences, Institut Teknologi Bandung, Jl. Ganesha No. 10, Bandung 40132, Indonesia*

[6]*Research Center for Nanosciences and Nanotechnology, Institut Teknologi Bandung, Jl. Ganesha No. 10, Bandung 40132, Indonesia*

* ***Corresponding author:***

email: nendenfauziah@uniga.ac.id

Received: July 16, 2025
Accepted: December 23, 2025

DOI: 10.22146/ijc.109307

Abstract: *Electrochemical synthesis can produce graphene-like materials containing structural defects, known as electrochemically exfoliated graphene (EEG), due to the presence of oxygen functional groups. These defects provide active sites for the adsorption of chromium ions. This study aims to determine the effect of voltage variation on the electrochemical exfoliation of graphite, specifically to identify the optimal voltage for producing EEG materials with the highest chromium adsorption capacity. We exfoliated graphite rods from dry-cell waste in a 0.2 M sulfuric acid solution at 5, 10, 15, and 20 V. The EEG was characterized with FTIR and Raman spectroscopy. The adsorption capacity was measured by AAS using 0.1 g of adsorbent in 10 mL of a 50 ppm Cr(VI) solution at pH 2 for 1 h. FTIR confirmed samples are reduced graphene oxide, showing hydroxyl, epoxy, carbonyl, carboxyl, and sulfonate groups. Raman spectroscopy revealed that EEG_15V was the most graphene-like, with the highest I_{2D}/I_D ratio. EEG_15V had the greatest Cr(VI) adsorption capacity at 5.27 mg/g.*

Keywords: *electrochemical exfoliation; graphene oxide (GO); adsorption; chromium (VI); battery waste*

■ INTRODUCTION

Human activities, such as leather tanning, textile dyeing, and wood preservation, have significantly contributed to environmental contamination with hexavalent chromium (Cr(VI)) [1]. Cr(VI) ions are highly toxic and pose serious risks to both human health and ecosystems. Prolonged exposure has been associated with oxidative stress [1-2], DNA damage [3], microcytic anemia, airway hypersensitivity, carcinogenic effects, and occupational asthma, as well as skin, eye, and respiratory tract irritation [2]. These adverse impacts highlight the urgent need to reduce Cr(VI) concentrations in water and wastewater.

Cr(VI) is highly toxic, carcinogenic, and mobile in aquatic systems, making it more toxic than other common pollutants. The risk of cancer from chromium exposure is higher over a lifetime than from Pb [4].

Compared to Cd, Cr(VI) has several additional toxic species and mechanisms (e.g., direct redox reactions) that make it more reactive and potentially a potent carcinogen, causing genetic damage [5]. The potential for exposure through the food chain is greater for Cr than for Cd under certain conditions [6]. Cr can cause more adverse biological effects than Cd in long-term conditions [7], so attention to Cr should be given priority.

One practical, low-cost way to treat water and reduce Cr(VI) ions is to use an adsorbent. Adsorption is widely regarded as one of the most effective techniques for chromium removal from aqueous systems due to its high efficiency, cost-effectiveness, and environmental compatibility. Unlike conventional methods such as chemical precipitation or coagulation, which are inefficient at trace concentrations and generate large volumes of toxic sludge, adsorption can effectively remove chromium even at very low concentrations with minimal secondary waste [8]. Moreover, adsorbents can be derived from low-cost or waste-based precursors, making the process economically viable and scalable [9]. The technique also offers operational simplicity, ease of regeneration, and the ability to tailor adsorbent surface chemistry to selectively target Cr(VI), further enhancing its applicability compared to ion exchange or membrane processes [10]. These advantages make adsorption the preferred method for sustainable chromium remediation.

A wide range of adsorbents, including activated carbon [11], silica-based materials [12], zeolites [13], clays [14], biopolymers [15], and graphene and its derivatives [16-19]. Graphene oxide (GO) [20-21] and reduced GO (rGO) [22] are particular graphene-like materials that can interact with metal ions because they contain oxygenated functional groups, such as hydroxyl (–OH), carbonyl (C=O), epoxy (C–O–C), and carboxyl (–COOH) [23]. These groups contribute to the adsorption of Cr(VI) [24-25], and computational studies have reported a strong adsorption energy of −143.80 kcal/mol [26]. The adsorption capacity of the GO material toward Cr(VI) ion was 41.27 mg/g [27]. In contrast, Mondal and Chakraborty [28] reported a much lower value of 1.222 μg/g. In contrast, rGO material yields 2.65 mg/g [22], indicating that adsorption performance can vary widely depending on synthesis methods, experimental conditions, and the type of material produced.

The common method used for GO and rGO synthesis is the Hummers' method [29-30]. The synthesis of GO/rGO using the Hummers' method involves the use of numerous chemicals, generating substantial chemical waste. A more eco-friendly method for synthesizing GO is electrochemical exfoliation [31]. Electrochemical exfoliation enables rapid exfoliation of graphite into GO sheets with tunable oxidation levels by adjusting the applied potential and electrolyte composition, offering greater control over defect density and functional group introduction [32]. Compared to chemical oxidants, this method reduces the generation of toxic byproducts, enables better control over defect density, functional group distribution, and sheet morphology, and is inherently more energy-efficient and suitable for scale-up [33].

Exfoliation of graphite can produce various carbon materials, including pristine graphene, heteroatom-doped graphene, and GO [19]. The electrochemical exfoliation process gives material, namely, electrochemically exfoliated graphene (EEG). EEG is a graphene-like material with various functional groups, including hydroxyl, carbonyl, epoxy, carboxyl, and S=O groups [34]. The exfoliation process is commonly used when a 10 V voltage is applied [31-32,34-35]. The voltage variation is predicted to result in different defect structures and varying numbers of layers. The defect structure and the number of graphene layers in the EEG can be analyzed using the Raman spectra. The Raman analysis in this study is discussed in more detail compared to previous reports by Fatya et al. [31] and Fauziah et al. [34], particularly in the fitting and deconvolution of the 2D peak using four Lorentzian components, which other researchers have not performed. These Raman analyses will yield data on differences in defect structure and the number of layers of EEG material, leading to different adsorption capacities for chromium ions.

To date, the use of EEG for Cr(VI) adsorption has not yet been systematically investigated. Meanwhile, EEG and other graphite-exfoliated materials have been

widely explored in diverse applications, including as counter electrodes in dye-sensitized solar cells [31,34], energy storage devices [36], transparent conductive films [37], organic dye adsorption [38], supercapacitors [39-40], lithium [41] and sodium batteries [42], electrochemical sensors [43], electrothermal heaters [44], and as functional components in high-temperature fuel cells [45]. These studies demonstrate the versatility of EEG and related materials, but their potential for heavy-metal adsorption remains underexplored. There has been no study of voltage variation in EEG synthesis that relates it to Raman analysis results, specifically regarding structural defects and the number of layers, which are associated with its adsorption capacity for Cr ions.

In this study, using waste zinc–carbon dry-cell batteries as a source of graphite offers an attractive strategy. These batteries are widely available as post-consumer waste, and recovering graphite from them not only reduces environmental pollution but also provides a low-cost, sustainable raw material for graphene synthesis. Thus, the valorization of waste batteries aligns with both environmental remediation and circular economy principles. The use of EEG material synthesized from graphite rods derived from dry-cell battery waste is therefore expected to provide a promising adsorbent for Cr(VI) ions.

■ EXPERIMENTAL SECTION

Materials

Chromium standard solution (1000 mg/L Cr, traceable to SRM from NIST, $Cr(NO_3)_3$ in 0.5 M HNO_3, Certipur®, Supelco/Merck, Germany), potassium dichromate ($K_2Cr_2O_7$, analytical grade, Merck, Germany), and sulfuric acid (H_2SO_4, 95–97%, analytical grade, Merck, Germany) were used in this work. Graphite rods for the exfoliation process were collected from spent zinc–carbon dry-cell batteries obtained from PT International Chemical Industry Co., Ltd., Indonesia. All reagents were of analytical grade and were used without further purification.

Instrumentation

Fourier-transform infrared (FTIR) spectra were acquired using a Bruker Alpha FTIR spectrometer. Raman spectra were recorded using a Bruker Senterra Raman spectrometer equipped with a 50× Olympus long-working-distance MPlan semiapochromat objective lens. Atomic absorption spectroscopy (AAS) measurements were performed using an Avanta Sigma A 6525 instrument.

Procedure

Synthesis of EEG

In EEG synthesis, the graphite rod was immersed in H_2SO_4 0.2 M solution inside a glass reactor. The Graphite rod was used as the electrode. Exfoliation was initiated by applying 3 V for 2 min, followed by 10 V for 60 min [31,34] using a DC adjustable power supply (60 V, 5 A, RXN-605D, ZHAOXIN). This process was repeated with applied voltages of 5, 15, and 20 V. Then, the obtained EEG for all voltage variations was collected by vacuum filtration and washed with distilled water. Finally, the EEG sample was dried in a vacuum oven for 1 h at 60 °C.

Characterizations

The molecular structures of the EEG sample were characterized using FTIR and Raman spectrometers. FTIR spectra were acquired using a Bruker Alpha FTIR spectrometer in transmission mode. EEG samples were prepared as KBr pellets and stored in a silica gel desiccator for 24 h to ensure that the pellets contained no water. Raman spectra were carried out using a Bruker Senterra Raman spectrometer equipped with a 50× Olympus long-working-distance MPlan semiapochromat objective lens. All samples were prepared on a gold surface and excited with a 532 nm Nd-YAG diode-pumped solid-state (DPSS) laser at 10 mW and an integration time of 40 s, with a co-addition of 2. The Raman spectra of the samples were fitted with Lorentzian functions to obtain peak positions, intensities, areas, and FWHMs.

Adsorption capacity analysis

The adsorption capacity analysis of the sample is performed using Atomic Absorption Spectroscopy on the Avanta Sigma A 6525 instrument. The AAS standard curve is created using concentrations of 0, 2, 5, 10, and 15 ppm, obtained by diluting a 1000 ppm AAS standard. For the adsorption of the sample, a 50 ppm Cr(VI)

solution was prepared by dissolving 0.141 g of $K_2Cr_2O_7$ (Merck) in 1 L of distilled water. 10 mL of Cr(VI) solution was placed in a 100 mL Erlenmeyer flask, and 0.1 g of the synthesized EEG was added. The EEG sample mixture was shaken for 1 h using an orbital shaker, CRYSTE PURIKER, at 150 rpm. The adsorption process was carried out at pH 2 [46-47]. The solution was then transferred to the centrifuge tube and centrifuged for 15 min at 150 rpm. The mixture was then filtered through Whatman 42 paper before measurement by an AAS instrument. The adsorption capacity (q) was calculated with Eq. (1);

$$q = \frac{(C_i - C_f)V_s}{m_a} \quad (1)$$

where q is the equilibrium adsorption capacity (mg adsorbate/g adsorbent), C_i is the initial concentration, C_f is the final concentration, V_s is the volume of the solution (liters), and m_a is the mass of the adsorbent (g) used [48].

■ RESULTS AND DISCUSSION

The graphite rod in the bottle of H_2SO_4 reagent produces bubbles when a 3 V voltage is applied (Fig. 1(a)). These bubbles are generated by water hydrolysis, indicating that the toolkit is functioning correctly. The scheme of the exfoliation process is presented in Fig. 1(b). When high voltage is applied (5, 10, 15, and 20 V), the water molecules are broken into radical species (HO•, H•, and •O•) [31,34]. The radical will interact with the C–C bond, then anchor to the graphite surface and form functional groups, such as hydroxyl, carbonyl, epoxy, and carboxyl. The anchored functional groups will cause the distance between the graphite layers, allowing sulfate ions to intercalate into this layer. The high voltage applied can also convert sulfate ions into SO_2 and O_2 gases; high pressure arises between the layers. The high pressure creates an explosion in the space between the layers [34]. The successful exfoliation of the graphite rod is evident from the solution turning dark after exposure to high voltage, as shown in Fig. 1(c). Exfoliation at 5 V takes 4 h to yield 0.2 g of an EEG sample. In comparison, 10, 15, and 20 V need 1 h, 40 and 20 min, respectively. The higher the applied voltage, the less exfoliation time required.

A comparison of the FTIR spectra between the graphite rod sample and the EEG sample, as shown in Fig. 2, demonstrates the success of synthesizing EEG from graphite rods. The EEG sample reveals the presence of functional groups, including hydroxyl, carbonyl, and epoxy. The presence of the OH functional

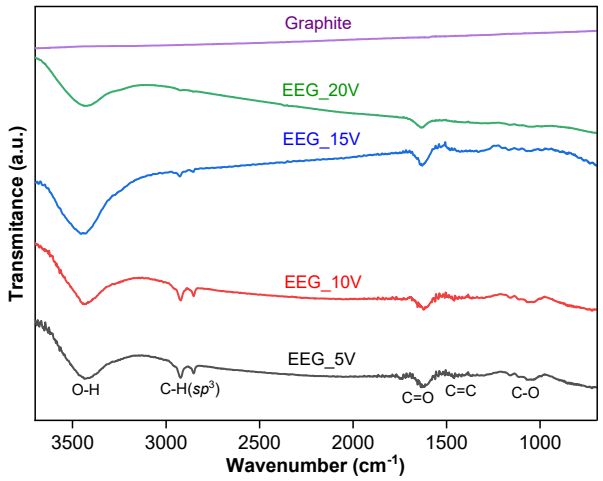

Fig 2. FTIR spectra of all samples, which show the electrochemical exfoliation process, reveal the introduction of several functional groups into the EEG compared to the pristine graphite rod

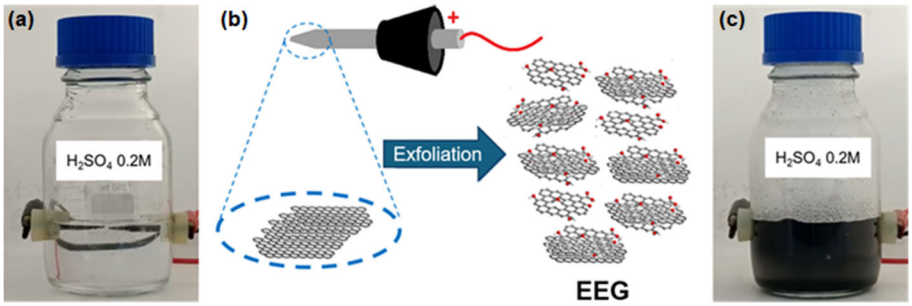

Fig 1. (a) Condition of the reaction bottle before high voltage is applied, (b) graphite rod exfoliation scheme, (c) condition of the reaction bottle after high voltage is applied

group is indicated by the presence of the broad peaks at 3100–3570 cm^{-1} [34,49], C=O groups with the peaks at 1700–1725 cm^{-1} [49], the stretching of the C–O aromatic group with the peaks at 1230–1270 cm^{-1} [50], and C=C strain on the aromatic ring with peaks at 1580–1615 cm^{-1} [49-50]. This FTIR data is also similar to that of GO from Ghul and Alrobei [49]. Fig. 2 also shows S=O groups in the form of a sulphate ester, with an intense band at 1223 cm^{-1} [34].

In electrochemical exfoliation, applying a higher voltage drives stronger oxidation of graphite layers. This generates more oxygen-containing functional groups (–OH, –C=O, –COOH, –O–) on the graphene surface. Since IR absorption bands correspond to these groups, their peaks become stronger as their populations increase. As oxidation proceeds, bonds become more polar (C–C → C–O, C=O). The change in dipole moment during vibration increases, directly amplifying the IR peak intensity. Higher voltage not only promotes exfoliation but also creates structural defects. Defects often terminate with polar functional groups (C–O, C=O). More defects will lead to more IR-active sites, thereby increasing the absorption intensity.

The FTIR spectra of the sample show that applying a 15 V voltage significantly increases peak intensity, particularly for the hydroxyl and carbonyl groups. The higher the voltage applied, the more likely it is that the number of radicals formed will increase. The more radicals that are formed, the more functional groups will be bound to the surface of the graphene layer. The higher voltage applied will result in more functional groups attaching to the graphene surface. Increasing the number of –OH groups in EEG_15V is predicted to enhance the material's interaction with Cr ions. The –OH group, which donates electrons, forms strong bonds with Cr ions and significantly enhances the adsorption capacity of adsorbents for Cr ions [25]. In addition, increasing the number of C=O groups in EEG_15V is predicted to improve the material's interaction with Cr ions. The C=O group plays a significant role in the adsorption of Cr ions, enhancing the adsorbent's capacity to remove it from aqueous solutions [24]. Moreover, COOH groups play a crucial role in Cr ion adsorption by providing active sites for ion exchange and complexation, thereby significantly enhancing the adsorption capacity of various adsorbents [24-25].

The Raman spectra in Fig. 3(a) also support the successful synthesis of EEG from graphite rods. The graphite rods exhibit a spectral shape with a low D (disorder) peak with a high and sharp G (Graphitic) peak. The Raman spectra of EEG with voltage applied of 5 V (EEG_5V), 10 V (EEG_10V), 15 V (EEG_15V), and 20 V (EEG_20V) show the typical spectral features with the broad and intense D band, the broad G band, and the hardly visible 2D band that is typically of graphene oxide or reduced graphene oxide material [29,34]. With a broader G band and a strong D band, there has been a change in the structure of the material due to the presence

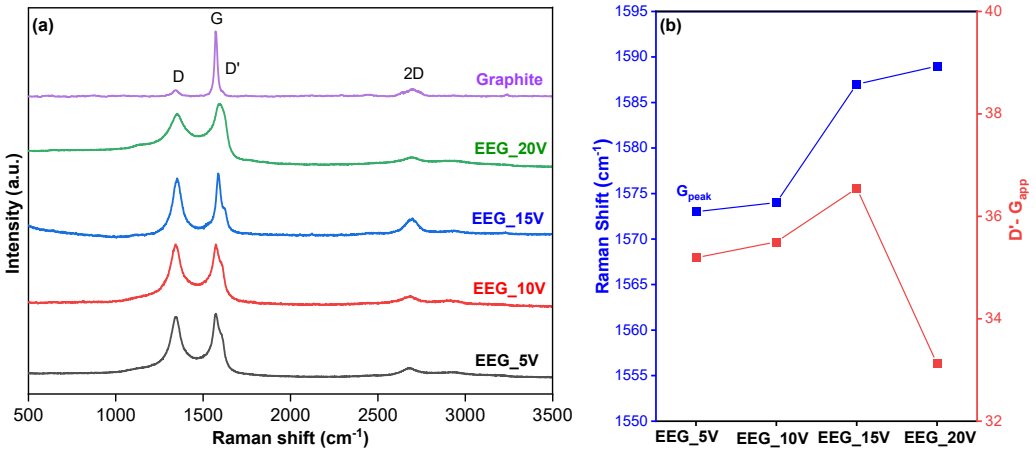

Fig 3. (a) Raman spectra of all samples compared to the pristine graphite rod and (b) plot of G peak position and D'-G_{app} value of all samples

of oxygen or other functional groups bound in the graphite structure. The G peak positions of EEG_5V, EEG_10V, EEG_15V, and EEG_20V are 1572, 1574, 1587, and 1589 cm^{-1}, respectively.

As shown in Fig. 3(b), the peak position shifts to higher values with increasing applied voltage. The EEG_5V and EEG_10V samples have G (1572–1574 cm^{-1}) peaks that are lower than those of standard graphene (~1585 cm^{-1}) [51]. The EEG_15V and EEG_20V exhibit a blue-shifted position, indicating that this sample has a more functional group attached to the graphene structure. This Raman result aligns with the FTIR result, indicating that EEG_15V and EEG_20V exhibit stronger peaks, particularly in the –OH and C=O regions. A companion peak around 1600–1626 cm^{-1} [52], commonly referred to as the D' peak, also appears. This peak shows the formation of defects in EEG material [52-53]. The difference between the D' peak position and the G_{app} (appearance) peak position can be used to predict the classification of EEG samples as GO, rGO, or graphene [34]. The value of D'–G_{app} < 0 is equal to C/O < 10, which means the carbon material is in graphene oxide form. If the D'–G_{app} value is in the range of 0 to 25, it is equal to C/O in the range of 10 to 500, and the carbon material is in rGO form [52], while if the D'–G_{app} > 25, then the material is more graphene-like [34]. The D'–G_{app} values of EEG_5V (35), EEG_10V (35), EEG_15V (37), and EEG_20V are graphene-like, with EEG_15V being the most graphene-like.

The D′ peak position comes from the fitting of the D and G peaks, as shown in Fig. 4(a–d) [34,51]. The G peak corresponds to in-plane carbon-atom stretching vibrations [54]. The G peak corresponds to sp^2 carbon, and the higher its intensity, the larger the sp^2 area in graphene-like materials [55]. The D peak indicates the degree of disorder in the carbon materials [56]. The activation of defects in the hexagonal rings of a graphene-like material gives rise to the D peak [57]. The higher the peak intensity of D peaks, the bigger the defect area in the graphene-like material. Therefore, the intensity ratio between the D and G peaks reflects the degree of defect in the graphene-like material [58]—the intensity ratio of the D to G peak for all samples.

Fig. 5(a) shows that the I_D/I_G of EEG_20V (0.86) < EEG_5V (1.01) < EEG_10V (1.07) < EEG_15V (1.09).

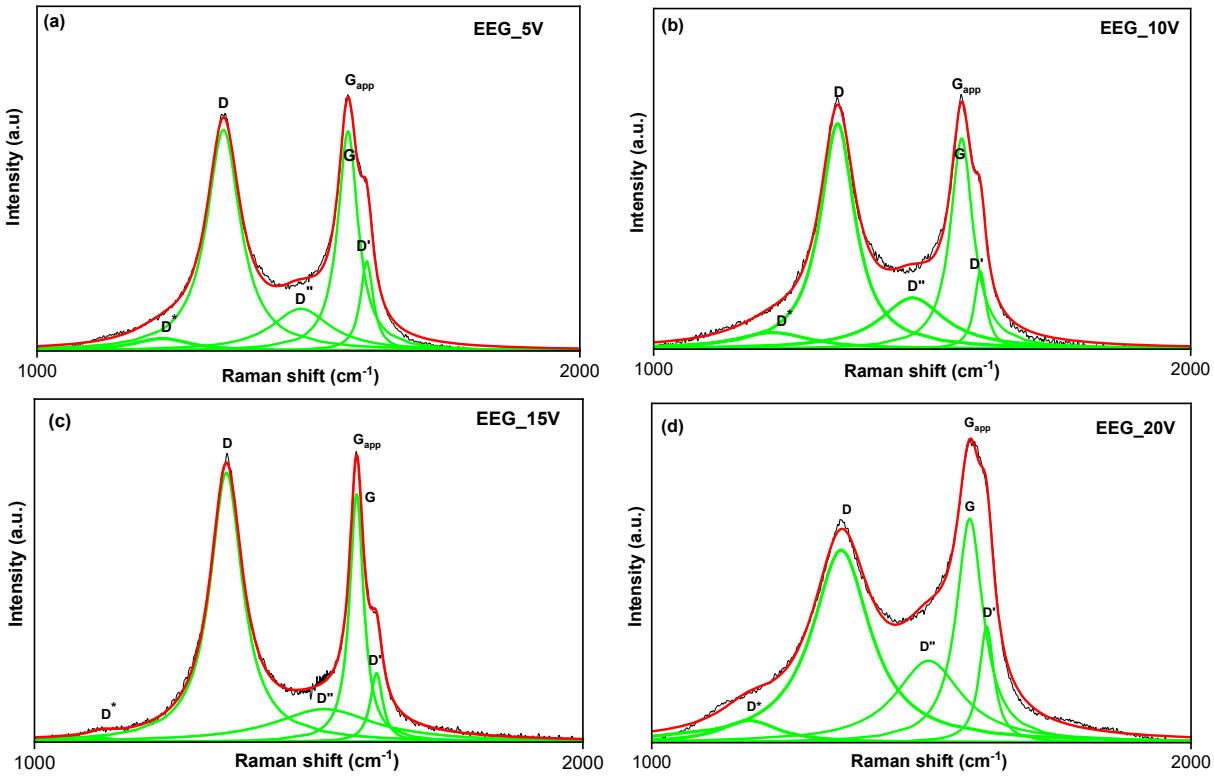

Fig 4. Fitting D and G peaks of Raman spectra of (a) EEG_5V, (b) EEG_10V, (c) EEG_15V and (d) EEG_20V

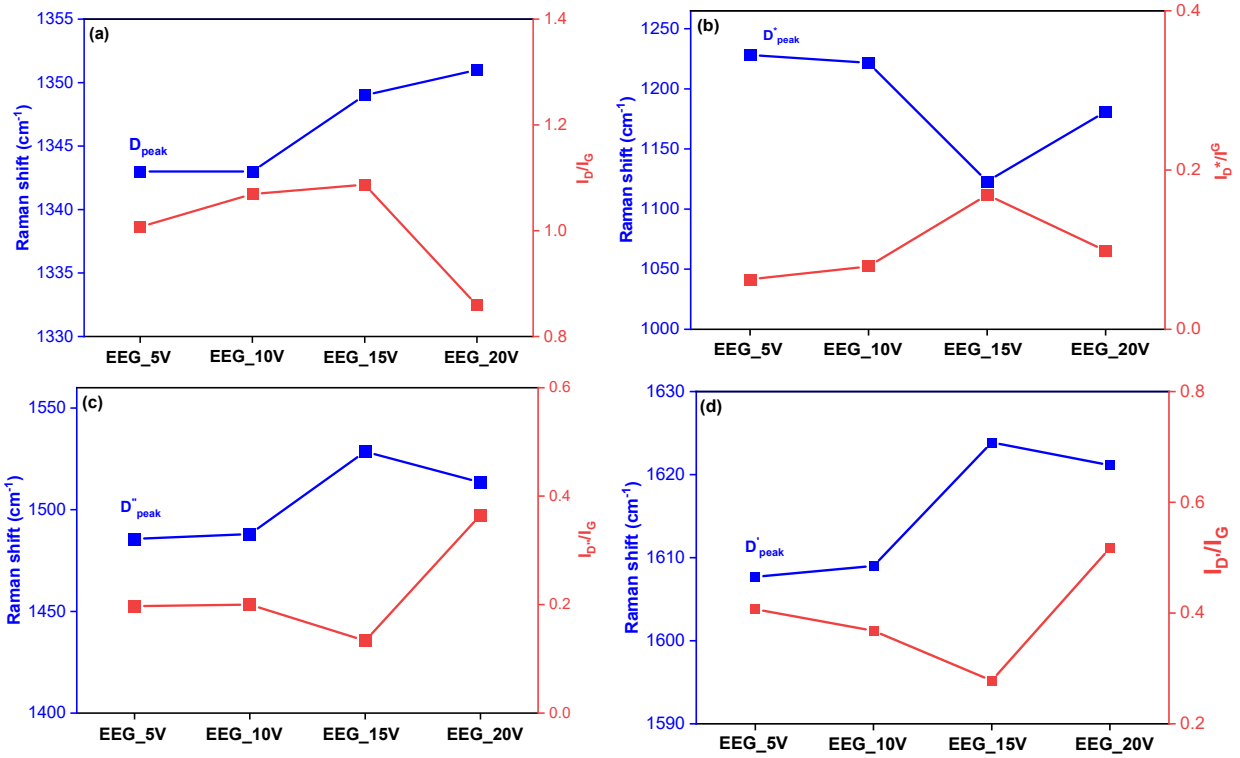

Fig 5. All sample plotting of (a) D peak position and I_D/I_G value, (b) D* peak position and I_{D^*}/I_G value, (c) D'' peak position and $I_{D''}/I_G$ value, and (d) D' peak position and $I_{D'}/I_G$ value

The I_D/I_G for all EEG samples is higher than 0.85, while the I_D/I_G of graphite is just 0.09, showing the success of converting graphite to EEG (the fitting D and G peaks of Raman spectra of graphite were shown in Fig. S1 and Table S1). The applied voltage increases the defect in the sample up to 15 V, but at 20 V, the anomaly occurs. Increasing the voltage applied during graphite exfoliation increases the defect density, which reaches a maximum at 15 V. The higher the defect density in graphene-like materials, the more active adsorption sites there are, so EEG_15V is the best candidate as an adsorbent agent. Fig. 5(a) also represents the peak position of the sample as the applied voltage varies. The D peak position of EEG_5V (1343 cm^{-1}), EEG_10V (1343 cm^{-1}), EEG_15V (1350 cm^{-1}), and EEG_20V (1351 cm^{-1}). The D peak, which usually appears at 1350 cm^{-1} [59]. It can be used to indicate irregularities in the sp^2 structure, such as the formation of C–H sp^3 bonds. Disturbances to the sp^2 structure will shift the D peak position to a lower frequency (redshift). The red shift in the D peak position of EEG_5V and EEG_10V because of the formation of C–H sp^3 is supported by FTIR spectra with peaks at 2800 and 2900 cm^{-1} that are more intense than those of EEG_15V and EEG_20V.

The D* peak is a small peak at 1200 cm^{-1} [34,51]. Fig. 5(b) shows that increasing the applied voltage causes a red shift in the D* peak position, even though EEG_20V is still larger than EEG_15V. This peak is related to a disordered graphitic lattice due to the presence of sp^3 bonds [51]. The D* peak position for EEG_5V at 1228 cm^{-1} is the reference position with the most regular structure or the least defects. EEG_10V at 1222 cm^{-1}, with 6 cm^{-1} redshift, indicates the occurrence of a slight increase in chemical disorder or defect. EEG_15V at 1123 cm^{-1}, with 105 cm^{-1} redshift, shows a high level of disorder, possibly caused by the disruption of many oxygen functional groups. Meanwhile, EEG_20V at 1181 cm^{-1}, with a 47 cm^{-1} redshift, shows moderate disorder, perhaps indicating a chemical modification. The I_{D^*}/I_G value is related to some functional groups (such as C–O sp^3) that attach to the graphene structure [51]. The trend of changes in the

value of I_{D*}/I_G for the sample in Fig. 5(b) is as follows: EEG_5V (0.06) < EEG_10V (0.08) < EEG_20V (0.10) < EEG_15V (0.18). The trend of I_{D*}/I_G increases with the increase in voltage applied, except for 20 V. This data can be interpreted as indicating that the condition in which EEG_5V has the least functional group compared to EEG_10V. In contrast, EEG_15V has the highest functional group (C–O sp^3) content. EEG_20V has more functional group content than EEG_5V and EEG_10V, but less than EEG_15V. The higher C–O sp^3 content in EEG_15V and EEG_20V compared to EEG_5V and EEG_10V is consistent with the FTIR spectra.

The D' peak (~1600–1625 cm^{-1}) is a resonance of the D mode. It is sensitive to disorder and structural defects in the sp^2 carbon system [60]. Fig. 5(c) shows that the D' peak position shifts to lower energy with increasing applied voltage. While the $I_{D'}/I_G$ have the order of $I_{D'}/I_G$ of EEG_15V < EEG_10V < EEG_5V < EEG_20V. The EEG_5V (1608 cm^{-1}), as a reference position, with $I_{D'}/I_G$ value of 0.41, has a moderate disorder; the sp^2 structure is relatively preserved, but it may have the lowest functional group content. The EEG_10V (1609 cm^{-1}), with $I_{D'}/I_G$ value of 0.41, has almost the same peak position but has experienced a slight increase in possible functional group content. However, the sp^2 structure is relatively more preserved than that of EEG_5V. The EEG_15V (1624 cm^{-1}) has the highest blueshift, which indicates the highest possible functional group content, but with the lowest $I_{D'}/I_G$ value (0.28), it shows the weakest defects in the sp^2 carbon system.

We can interpret this data as a phenomenon: the increase in functional group attachment without an increase in defects in the sp^2 carbon system. This is probably because the functional group is attached to the edge of the graphitic structure of the EEG material. While EEG_20V (1621 cm^{-1}) has a high blueshift, indicating that the disorder increased significantly with the highest $I_{D'}/I_G$ value (0.52), showing that it shows a very high disorder, the structure is very disturbed by heavy oxidation/functionalization. The 20 V voltage applied makes the EEG material more amorphous due to the presence of the broad peak D" peak at 1350 cm^{-1} with the highest $I_{D''}/I_G$ value (Fig. 5(d)). The D" peak is related to amorphous phases [34].

The peak at 2700 cm^{-1} is known as the 2D peak, the second-order derivative of the D peak [61]. The fitting of the 2D peak uses four Lorentzian functions to give 3 other peaks named D+D" [62], D+G and 2G [34], as we can see in Fig. 6(a–d). The fitting results in Fig. 6 show the pattern of changes in the peak ratio values of I_{2D}/I_G and FWHM (Fig. 7(a)), and the D+D" peak position and the ratio of $I_{D+D''}/I_G$ (Fig. 7(b)). The higher value of I_{2D}/I_G confirms a highly crystalline structure [63]. The EEG_15V shows a higher I_{2D}/I_G ratio, indicating it is more crystalline than the other sample. The value in Fig. 7(a) increases with increasing voltage; the anomaly is also evident in the EEG sample with 20 V applied. The comparison of the intensity of the 2D peak to the G peak can also be used to predict the number of layers [34]. The value of I_{2D}/I_G for monolayer graphene is 2, while for bilayer graphene, it is 1; subsequently, multilayer graphene yields $I_{2D}/I_G > 1$ [64-65]. All samples have values less than 1, indicating that they are multilayer graphene. However, EEG_15V has the highest value, suggesting it has the fewest layers. This result also aligns with the FWHM values extracted from the 2D peak fit. The EEG_15V with the smallest FWHM is assigned the smallest layer number. The lower the graphene layer number, the higher the adsorption capacity [34]. The EEG_15 is the best candidate for an EEG sample as an adsorption agent for chromium ions.

The increasing voltage applied shows that the phenomenon increases with increasing local disorder, indicating that edge modification has occurred without damaging the overall sp^2 structure [60]. The edge modification can be studied by analyzing the D+D" peak, which is indicative of defect-activated or edge modification [62]. The D+D" peak is observed at 2450 cm^{-1} [40]. Then, the ratio of the intensity of the D+D" peak to the intensity of the 2D peak shows the edge modification degree. The plot of the value of $I_{D+D''}/I_G$ for all samples in Fig. 7(b) shows that the $I_{D+D''}/I_G$ is increased due to the increase in voltage applied, except for 20 V. This data indicates that increasing the applied voltage from 5 to 15 V increases local disorder without damaging the overall sp^2 structure. The D+G peak is

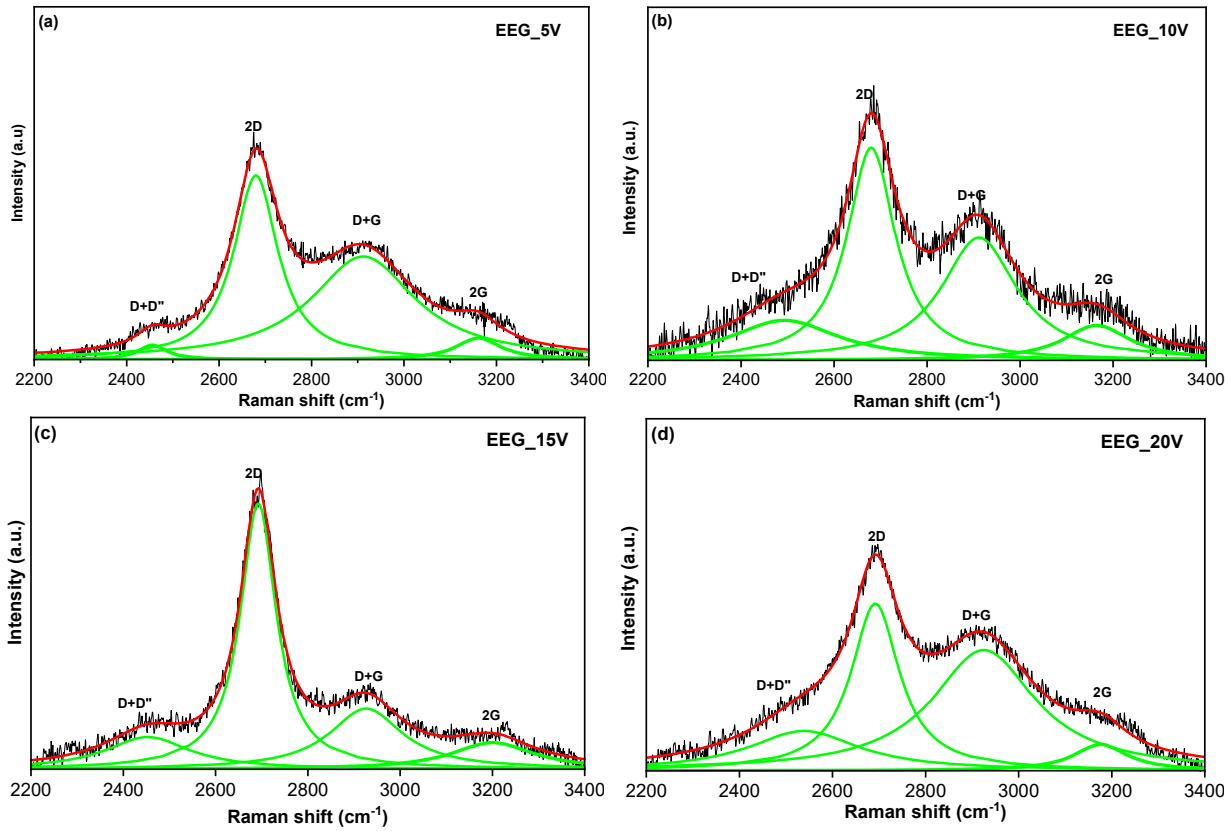

Fig 6. Fitting 2D peaks of Raman spectra of (a) EEG_5V, (b) EEG_10V, (c) EEG_15V, and (d) the EEG_20V sample

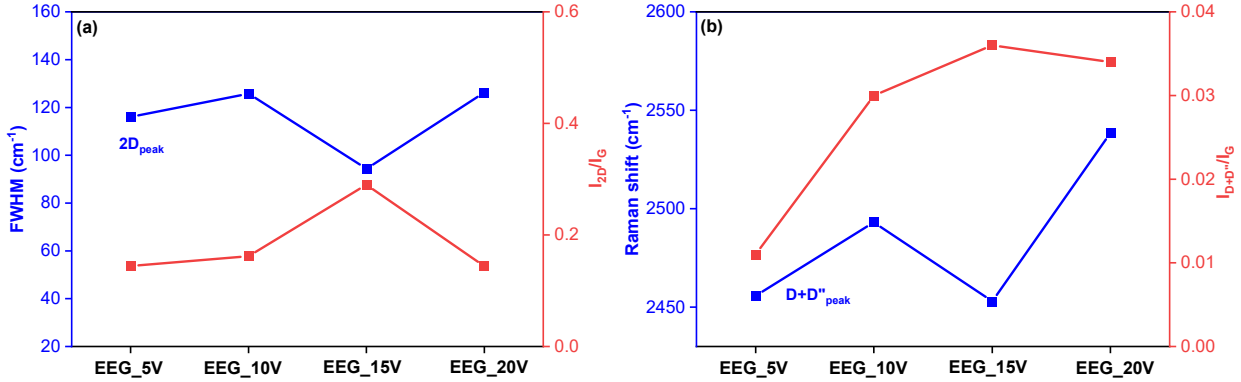

Fig 7. Plotting Raman data of (a) FWHM 2D peak and the ratio of I_{2D}/I_G, and (b) D+D" peak position and the ratio of $I_{D+D"}/I_G$

visible at 2950 cm^{-1} [60,62], a defect-activated peak [62] not directly related to edge modification. This peak is attributed to asymmetric C–H stretching in CH_3/CH_2 groups attached to sp^3 sites [66], indicating the presence of C–H (hydrogenated amorphous carbon). The presence of C–H sp^3 is confirmed with the presence of the peaks at 2800 and 2900 cm^{-1} in the FTIR spectra.

Raman analysis indicates that the EEG_15V is the best candidate for the adsorbent agent. The results of the adsorption capacity test of EEG samples against Cr(VI) ions showed that the adsorption power of the EEG_5V sample was 4.38 mg/g, EEG_10V was 4.58 mg/g, EEG_15V was 5.27 mg/g, and EEG_20V was 3.29 mg/g. EEG_15V has the highest adsorption capacity, as predicted previously. By using Eq. (2) [67], the defect density (nD) value of EEG_5V is 3.02×10^{-11} cm^{-2},

EEG_10V is 3.20×10^{-11} cm^{-2}, EEG_15V is 3.26×10^{-11} cm^{-2}, and EEG_20V is 2.57×10^{-11} cm^{-2}. In the plot in Fig. 8, the higher the defect density, the higher the adsorption capacity. EEG_15V has the highest adsorption due to its higher defect density.

The relationship between defect density and the adsorption capacity of carbon materials is supported by research by You et al. [68], which shows that structural defects make the graphene surface more active in adsorbing gases such as NO_2. Other research has shown that only defective graphene can adsorb oxygen, whereas pristine graphene does not [69]. The poor defect in the graphene structure results in the lower adsorption capacity of Li [70]. It means the higher the defect density of the graphene material, the higher the adsorption capacity. EEG_15V, with the highest defect density, is related to the number of functional groups that attach to the graphene structure of EEG_15V. The EEG_15V shows a high intensity of –OH groups, as indicated by the FTIR result. The number of –OH groups bound to the EEG_15V sample will form strong bonds with Cr ions and significantly enhance the adsorption capacity [25]. The FTIR data also show that EEG_15V has a high C=O content, which enhances the adsorbent's capacity to remove Cr from aqueous solutions. The presence of –OH, C=O, and epoxy groups is vital to the adsorption process, as they serve as adsorption sites for dichromate ions ($Cr_2O_7^{2-}$). The interaction mechanism of the Cr metal adsorption process on the graphene material is adsorbed through noncovalent van der Waals forces, with a computational study using DFT and molecular modeling giving the adsorption energy ranges from around −133.7 to −143.8 kcal/mol depending on the specific functional group (hydroxyl, epoxy, carboxyl) at the adsorption site [26].

$$nD = \frac{2.4\times10^{22}}{\lambda_L^4}\left(\frac{I_D}{I_G}\right) \quad (2)$$

$$n = \frac{2\times I_G}{I_{2D}} \quad (3)$$

The monolayer of graphene has an I_{2D}/I_G value of 2, so we assume that the number of layers of the EEG can be counted using Eq. (3). The number of layers (n) of EEG_15V (~7) < EEG_10V (~12) < EEG_5V(~13) < EEG_20V (~14). If we assume that the graphite rod source

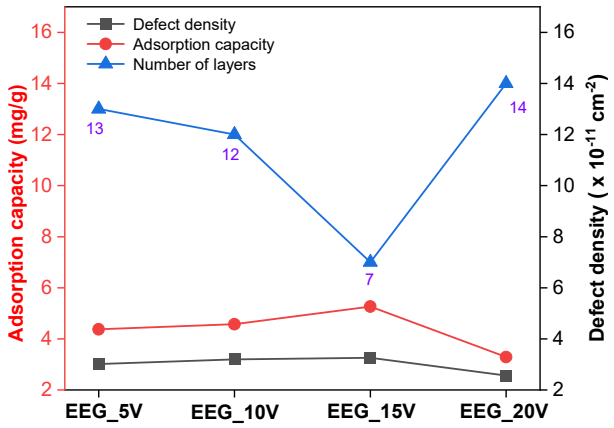

Fig 8. Plotting of defect density, adsorption capacity, and number of layers in all samples

in the exfoliation process has the same number of layers as 7.644 layers of graphene, then in EEG_15 will be the 2.184 active surface for adsorption, while in EEG_10V is 1.274, in EEG_5V is 1.176, and in EEG_20V is 1.092. The more active the surface, the higher the adsorption capacity [71]. EEG_15V has the fewest layers, resulting in a higher adsorption capacity, as adsorption capacity increases with fewer graphene layers. Here, we can say that EEG_15V has the highest adsorption capacity due to its lower number of layers and higher defect structure. The EEG_15V adsorption capacity is lower than that of the GO material, with a maximum adsorption capacity of Cr(VI) of 41.27 mg/g [27]. Still, it is higher than that of pure rGO, with an adsorption capacity for Cr(VI) metal ions of 2.65 mg/g [22]. EEG material is a graphene-like material closer to rGO than to GO [32,34]. rGO has lower defects than GO, which results in the rGO material having a lower adsorption capacity for Cr(VI) than the GO material.

■ CONCLUSION

The results showed that the EEG with a 15 V voltage variation produced a material with the highest structural defects and the fewest layers, thereby having the greatest impact on the adsorption capacity of Cr(VI) ions. EEG_15V was able to adsorb 5.27 mg/g of Cr(VI) ions in a 1-h adsorption process. The low adsorption capacity of EEG material can be increased through several modification steps, such as activation via soaking in residual solvents or by forming a composite with conductive polymers, such as polyaniline, or with

transition-metal compounds, such as MnO_2. However, the research objective of obtaining the optimum voltage to produce a material with potential as a cheap and efficient adsorbent from used battery waste has been achieved. This finding has the potential to enable efficient, environmentally friendly processing of small-scale industrial waste. This research is still limited to a laboratory scale and has not been tested on real waste. Further research is needed to test the effectiveness of this adsorbent in continuous systems and under field conditions. Replacing H_2SO_4 with a more environmentally friendly exfoliation medium is another crucial step in this research.

■ ACKNOWLEDGMENTS

This research was funded by a grant from the Faculty of Mathematics and Natural Sciences. Therefore, the author would like to express her gratitude to the Dean, the head of the laboratory, and all the staff of the Faculty of Mathematics and Natural Sciences of Universitas Garut for providing the facilities and infrastructure necessary for this research.

■ CONFLICT OF INTEREST

The authors declare no competing financial interests or personal relationships that may have influenced the work reported in this study.

■ AUTHOR CONTRIBUTIONS

Nenden Fauziah: Writing – original draft, Visualization, Formal analysis, Data curation, Investigation, Project administration, Funding acquisition, Conceptualization. Rini Febi Nuraeni: Investigation, Formal analysis, Visualization, Data Curation. Validation. Fitri Dara: Formal analysis, Validation. Rafiq Arsyad: Resources. Nadiatus Silmi: Formal analysis, Visualization. Veinardi Suendo: Writing – review & editing, Supervision.

■ REFERENCES

[1] Xie, S., 2024, Water contamination due to hexavalent chromium and its health impacts: Exploring green technology for Cr (VI) remediation, *Green Chem. Lett. Rev.*, 17 (1), 2356614.

[2] Mohanty, S., Benya, A., Hota, S., Kumar, M.S., and Singh, S., 2023, Eco-toxicity of hexavalent chromium and its adverse impact on environment and human health in Sukinda Valley of India: A review on pollution and prevention strategies, *Environ. Chem. Ecotoxicol.*, 5, 46–54.

[3] Krawic, C., and Zhitkovich, A., 2023, Chemical mechanisms of DNA damage by carcinogenic chromium(VI), *Adv. Pharmacol.*, 96, 25–46.

[4] Widyantoro, A., Maziya, F.B., and Abidin, A.U., 2021, Exposure analysis of lead (Pb) and chromium (Cr) in workplace workshop PT. X, *Gac. Sanit.*, 35, S450–S454.

[5] Rahman, Z., and Singh, V.P., 2019, The relative impact of toxic heavy metals (THMs) (arsenic (As), cadmium (Cd), chromium (Cr)(VI), mercury (Hg), and lead (Pb)) on the total environment: An overview, *Environ. Monit. Assess.*, 191 (7), 419.

[6] Usman, K., Al Jabri, H., Abu-Dieyeh, M.H., and Alsafran, M.H.S.A., 2020, Comparative assessment of toxic metals bioaccumulation and the mechanisms of chromium (Cr) tolerance and uptake in *Calotropis procera*, *Front. Plant Sci.*, 11, 883.

[7] Freitas, E.C., and Rocha, O., 2014, Acute and chronic toxicity of chromium and cadmium to the tropical cladoceran *Pseudosida ramosa* and the implications for ecotoxicological studies, *Environ. Toxicol.*, 29 (2), 176–186.

[8] Owlad, M., Aroua, M.K., Wan Daud, W.A., and Baroutian, S., 2009, Removal of hexavalent chromium-contaminated water and wastewater: A review, *Water, Air, Soil Pollut.*, 200 (1), 59–77.

[9] Babel, S., and Kurniawan, T.A., 2003, Low-cost adsorbents for heavy metals uptake from contaminated water: A review, *J. Hazard. Mater.*, 97 (1-3), 219–243.

[10] Saha, B., and Orvig, C., 2010, Biosorbents for hexavalent chromium elimination from industrial and municipal effluents, *Coord. Chem. Rev.*, 254 (23-24), 2959–2972.

[11] Wang, Y., Peng, C., Padilla-Ortega, E., Robledo-Cabrera, A., and López-Valdivieso, A., 2020, Cr(VI) adsorption on activated carbon: Mechanisms,

modeling and limitations in water treatment, *J. Environ. Chem. Eng.*, 8 (4), 104031.

[12] Mallik, A.K., Moktadir, M.A., Rahman, M.A., Shahruzzaman, M., and Rahman, M.M., 2022, Progress in surface-modified silicas for Cr(VI) adsorption: A review, *J. Hazard. Mater.*, 423, 127041.

[13] Neolaka, Y.A.B., Lawa, Y., Naat, J., Riwu, A.A.P., Mango, A.W., Darmokoesoemo, H., Widyaningrum, B.A., Iqbal, M., and Kusuma, H.S., 2022, Efficiency of activated natural zeolite-based magnetic composite (ANZ-Fe_3O_4) as a novel adsorbent for removal of Cr(VI) from wastewater, *J. Mater. Res. Technol.*, 18, 2896–2909.

[14] Rathnayake, S.I., Martens, W.N., Xi, Y., Frost, R.L., and Ayoko, G.A., 2017, Remediation of Cr (VI) by inorganic-organic clay, *J. Colloid Interface Sci.*, 490, 163–173.

[15] Shekhawat, A., Kahu, S., Saravanan, D., Pandey, S., and Jugade, R., 2022, Rational modification of chitosan biopolymer for remediation of Cr(VI) from water, *J. Hazard. Mater. Adv.*, 7, 100123.

[16] Khalajiolyaie, A., and Jian, C., 2025, Advances in graphene-based materials for metal ion sensing and wastewater treatment: A review, *Environments*, 12 (2), 43.

[17] Li, G., Du, R., Cao, Z., Li, C., Xue, J., Ma, X., and Wang, S., 2024, Research progress in graphene-based adsorbents for wastewater treatment: Preparation, adsorption properties and mechanisms for inorganic and organic pollutants, *C*, 10 (3), 78.

[18] Huang, J., Cui, W., Liang, R., Zhang, L., and Qiu, J., 2021, Porous BMTTPA-CS-GO nanocomposite for the efficient removal of heavy metal ions from aqueous solutions, *RSC Adv.*, 11 (6), 3725–3731.

[19] Smith, A.T., LaChance, A.M., Zeng, S., Liu, B., and Sun, L., 2019, Synthesis, properties, and applications of graphene oxide/reduced graphene oxide and their nanocomposites, *Nano Mater. Sci.*, 1 (1), 31–47.

[20] Melchor-Durán, A.P., Moreno-Virgen, M.R., Bonilla-Petriciolet, A., Reynel-Ávila, H.E., Lucio Ortiz, E., and González-Vázquez, O.F., 2024, Heavy metal removal from water using graphene oxide in magnetic-assisted adsorption systems: Characterization, adsorption properties, and modelling, *Separations*, 11 (10), 294.

[21] Jawad, N.A., and Naife, T.M., 2023, Removal of heavy metal ions from aqueous solution by nano graphene oxide, *Chem. Chem. Technol.*, 17 (4), 894–902.

[22] Philip, R.S., Aparna, N., and Mathew, M., 2024, Hexavalent chromium removal using reduced graphene oxide-zinc oxide composite fabricated via simple pyrolysis method, *Appl. Surf. Sci. Adv.*, 19, 100535.

[23] Gonçalves, M.G., Costa, V.O., Martinez, A.H.G., Régnier, B.M., Gomes, G.C.B., Zarbin, A.J.G., and Orth, E.S., 2024, Functionalization of graphene oxide via epoxide groups: A comprehensive review of synthetic routes and challenges, *Front. Carbon*, 3, 1393077.

[24] Lach, J., and Okoniewska, E., 2023, Adsorption of chromium and nickel ions on commercial activated carbon—An analysis of adsorption kinetics and statics, *Molecules*, 28 (21), 7413.

[25] Gao, C., Dong, Z., Hao, X., Yao, Y., and Guo, S., 2020, Preparation of reduced graphene oxide aerogel and its adsorption for Pb(II), *ACS Omega*, 5 (17), 9903–9911.

[26] Alija, A., Gashi, D., Plakaj, R., Omaj, A., Thaçi, V., Reka, A., Avdiaj, S., and Berisha, A., 2020, A theoretical and experimental study of the adsorptive removal of hexavalent chromium ions using graphene oxide as an adsorbent, *Open Chem.*, 18 (1), 936–942.

[27] Khdoor, Z., Makharza, S., Qurie, M., Fohely, F., Abu Taha, A., and Hampel, S., 2024, Removal of toxic hexavalent chromium via graphene oxide nanoparticles: Study of kinetics, isotherms, and thermodynamics, *RSC Adv.*, 14 (34), 24345–24351.

[28] Mondal, N.K., and Chakraborty, S., 2020, Adsorption of Cr(VI) from aqueous solution on graphene oxide (GO) prepared from graphite: Equilibrium, kinetic and thermodynamic studies, *Appl. Water Sci.*, 10 (2), 61.

[29] Sunarya, R.R., Hidayat, R., Radiman, C.L., and Suendo, V., 2020, Electrocatalytic activation of a DSSC graphite composite counter electrode using

in situ polymerization of aniline in a water/ethanol dispersion of reduced graphene oxide, *J. Electron. Mater.*, 49 (5), 3182–3190.

[30] Guerrero-Contreras, J., and Caballero-Briones, F., 2015, Graphene oxide powders with different oxidation degree, prepared by synthesis variations of the Hummers method, *Mater. Chem. Phys.*, 153, 209–220.

[31] Fatya, A.I., Reza, M., Sunarya, R.R., and Suendo, V., 2020, Synthesis of polyaniline/electrochemically exfoliated graphene composite as counter-electrode in dye-sensitized solar cell, *Polym.-Plast. Technol. Mater.*, 59 (12), 1370–1378.

[32] Parvez, K., Li, R., Puniredd, S.R., Hernandez, Y., Hinkel, F., Wang, S., Feng, X., and Müllen, K., 2013, Electrochemically exfoliated graphene as solution-processable, highly conductive electrodes for organic electronics, *ACS Nano*, 7 (4), 3598–3606.

[33] Salverda, M., Thiruppathi, A.R., Pakravan, F., Wood, P.C., and Chen, A., 2022, Electrochemical exfoliation of graphite to graphene-based nanomaterials, *Molecules*, 27 (24), 8643.

[34] Fauziah, N., Silmi, N., Nugroho, F.G., Putra, K.L.H., Benu, D.P., Steky, F.V., Sunarya, R.R., Yuliarto, B., Hidayat, R., and Suendo, V., 2023, Ultrasonication-modified electrochemically exfoliated graphene for counter electrode in dye-sensitized solar cells, *Carbon Trends*, 12, 100292.

[35] Tuzemen, G.B., 2024, Production of graphene by electrochemical exfoliation method and energy applications, *International Conference on Engineering, Natural Sciences, and Technological Developments (ICENSTED 2024)*, July 19–21, 2024.

[36] Ambrosi, A., and Pumera, M., 2016, Electrochemically exfoliated graphene and graphene oxide for energy storage and electrochemistry applications, *Chem. - Eur. J.*, 22 (1), 153–159.

[37] Marković, Z.M., Budimir, M.D., Kepić, D.P., Holclajtner-Antunović, I.D., Marinović-Cincović, M.T., Dramićanin, M.D., Spasojević, V.D., Peruško, D.B., Špitalský, Z., Mičušik, M., Pavlović, V.B., and Todorović-Marković, B.M., 2016, Semi-transparent, conductive thin films of electrochemical exfoliated graphene, *RSC Adv.*, 6 (45), 39275–39283.

[38] Ali, M.E.A., 2019, Preparation of graphene nanosheets by electrochemical exfoliation of a graphite-nanoclay composite electrode: Application for the adsorption of organic dyes, *Colloids Surf., A*, 570, 107–116.

[39] He, D., Marsden, A.J., Li, Z., Zhao, R., Xue, W., and Bissett, M.A., 2019, A single step strategy to fabricate graphene fibres via electrochemical exfoliation for micro-supercapacitor applications, *Electrochim. Acta*, 299, 645–653.

[40] Edison, T.N.J.I., Atchudan, R., Karthik, N., Chandrasekaran, P., Perumal, S., Arunachalam, P., Raja, P.B., Sethuraman, M.G., and Lee, Y.R., 2021, Electrochemically exfoliated graphene sheets as electrode material for aqueous symmetric supercapacitors, *Surf. Coat. Technol.*, 416, 127150.

[41] Zhao, X., Li, H., Han, F., Dai, M., Sun, Y., Song, Z., Han, D., and Niu, L., 2020, Electrochemical exfoliation of graphene as an anode material for ultra-long cycle lithium ion batteries, *J. Phys. Chem. Solids*, 139, 109301.

[42] Alhajji, E., Zhang, F., and Alshareef, H.N., 2021, Status and prospects of laser-induced graphene for battery applications, *Energy Technol.*, 9 (10), 2100454.

[43] Masemola, D.P., Mafa, P.J., Nyoni, H., Mamba, B.B., and Msagati, T.A.M., 2020, Gold nanoparticles modified exfoliated graphite electrode as electrochemical sensor in the determination of psychoactive drug, *J. Environ. Sci. Health, Part B*, 55 (5), 455–461.

[44] Han, J., Zhang, Y., Mei, J., Qiu, Z., Pan, K., Jiang, J., Zheng, F., Huang, Y., Wang, H., and Li, Q., 2024, Superior instant heating and electrothermal performances of interconnected graphene-expanded graphite-based electric heating composite, *ACS Appl. Nano Mater.*, 7 (11), 12579–12591.

[45] Chen, J., Perez-Page, M., Ji, Z., Zhang, Z., Guo, Z., and Holmes, S., 2021, One step electrochemical exfoliation of natural graphite flakes into graphene oxide for polybenzimidazole composite membranes giving enhanced performance in high temperature

fuel cells, *J. Power Sources*, 491, 229550.

[46] Rout, D.R., and Jena, H.M., 2023, Synthesis of graphene oxide-modified porous chitosan cross-linked polyaniline composite for static and dynamic removal of Cr(VI), *Environ. Sci. Pollut. Res.*, 30 (9), 22992–23011.

[47] Neolaka, Y.A.B., Lawa, Y., Naat, J.N., Riwu, A.A.P., Iqbal, M., Darmokoesoemo, H., and Kusuma, H.S., 2020, The adsorption of Cr(VI) from water samples using graphene oxide-magnetic (GO-Fe_3O_4) synthesized from natural cellulose-based graphite (kusambi wood or *Schleichera oleosa*): Study of kinetics, isotherms and thermodynamics, *J. Mater. Res. Technol.*, 9 (3), 6544–6556.

[48] Kaushal, A., and Singh, S.K., 2017, Critical analysis of adsorption data statistically, *Appl. Water Sci.*, 7 (6), 3191–3196.

[49] Gul, W., and Alrobei, H., 2021, Effect of graphene oxide nanoparticles on the physical and mechanical properties of medium density fiberboard, *Polymers*, 13 (11), 1818.

[50] Nandiyanto, A.B.D., Oktiani, R., and Ragadhita, R., 2019, How to read and interpret FTIR spectroscope of organic material, *Indones. J. Sci. Technol.*, 4 (1), 97–118.

[51] Claramunt, S., Varea, A., López-Díaz, D., Velázquez, M.M., Cornet, A., and Cirera, A., 2015, The importance of interbands on the interpretation of the Raman spectrum of graphene oxide, *J. Phys. Chem. C*, 119 (18), 10123–10129.

[52] King, A.A.K., Davies, B.R., Noorbehesht, N., Newman, P., Church, T.L., Harris, A.T., Razal, J.M., and Minett, A.I., 2016, A new Raman metric for the characterisation of graphene oxide and its derivatives, *Sci. Rep.*, 6 (1), 19491.

[53] López-Díaz, D., Delgado-Notario, J.A., Clericò, V., Diez, E., Merchán, M.D., and Velázquez, M.M., 2020, Towards understanding the Raman spectrum of graphene oxide: The effect of the chemical composition, *Coatings*, 10 (6), 524.

[54] Hao, Y., Wang, Y., Wang, L., Ni, Z., Wang, Z., Wang, R., Koo, C.K., Shen, Z., and Thong, J.T.L., 2010, Probing layer number and stacking order of few-layer graphene by Raman spectroscopy, *Small*, 6 (2), 195–200.

[55] Ferrari, A.C., and Robertson, J., 2000, Interpretation of Raman spectra of disordered and amorphous carbon, *Phys. Rev. B*, 61 (20), 14095–14107.

[56] Abid, A., Sehrawat, P., Islam, S.S., Mishra, P., and Ahmad, S., 2018, Reduced graphene oxide (rGO) based wideband optical sensor and the role of temperature, defect states and quantum efficiency, *Sci. Rep.*, 8 (1), 3537.

[57] Cançado, L.G., Jorio, A., Ferreira, E.H.M., Stavale, F., Achete, C.A., Capaz, R.B., Moutinho, M.V.O., Lombardo, A., Kulmala, T.S., and Ferrari, A.C., 2011, Quantifying defects in graphene via Raman spectroscopy at different excitation energies, *Nano Lett.*, 11 (8), 3190–3196.

[58] Hidayah, N.M.S., Liu, W.W., Lai, C.W., Noriman, N.Z., Khe, C.S., Hashim, U., and Lee, H.C., 2017, Comparison on graphite, graphene oxide and reduced graphene oxide: Synthesis and characterization, *AIP Conf. Proc.*, 1892 (1), 150002.

[59] Adetayo, A., and Runsewe, D., 2019, Synthesis and fabrication of graphene and graphene oxide: A review, *Open J. Compos. Mater.*, 9 (2), 207–229.

[60] Eckmann, A., Felten, A., Mishchenko, A., Britnell, L., Krupke, R., Novoselov, K.S., and Casiraghi, C., 2012, Probing the nature of defects in graphene by Raman spectroscopy, *Nano Lett.*, 12 (8), 3925–3930.

[61] Ferrari, A.C., 2007, Raman spectroscopy of graphene and graphite: Disorder, electron-phonon coupling, doping and nonadiabatic effects, *Solid State Commun.*, 143 (1-2), 47–57.

[62] De Silva, K.K.H., Viswanath, P., Rao, V.K., Suzuki, S., and Yoshimura, M., 2021, New insight into the characterization of graphene oxide and reduced graphene oxide monolayer flakes on Si-based substrates by optical microscopy and Raman spectroscopy, *J. Phys. Chem. C*, 125 (14), 7791–7798.

[63] Dong, L., Yang, J., Chhowalla, M., and Loh, K.P., 2017, Synthesis and reduction of large sized graphene oxide sheets, *Chem. Soc. Rev.*, 46 (23), 7306–7316.

[64] Ferrari, A.C., and Basko, D.M., 2013, Raman spectroscopy as a versatile tool for studying the

properties of graphene, *Nat. Nanotechnol.*, 8 (4), 235–246.

[65] Malard, L.M., Pimenta, M.A., Dresselhaus, G., and Dresselhaus, M.S., 2009, Raman spectroscopy in graphene, *Phys. Rep.*, 473 (5-6), 51–87.

[66] Robertson, J., 2002, Diamond-like amorphous carbon, *Mater. Sci. Eng. R Rep.*, 37 (4-6), 129–281.

[67] Kaushal, A., Dhawan, S.K., and Singh, V., 2019, Determination of crystallite size, number of graphene layers and defect density of graphene oxide (GO) and reduced graphene oxide (RGO), *AIP Conf. Proc.*, 2115 (1), 030106.

[68] You, Y., Deng, J., Tan, X., Gorjizadeh, N., Yoshimura, M., Smith, S.C., Sahajwalla, V., and Joshi, R.K., 2017, On the mechanism of gas adsorption for pristine, defective and functionalized graphene, *Phys. Chem. Chem. Phys.*, 19 (8), 6051–6056.

[69] Li, T., and Yarmoff, J.A., 2018, Defect-induced oxygen adsorption on graphene films, *Surf. Sci.*, 675, 70–77.

[70] Lee, E., and Persson, K.A., 2012, Li absorption and intercalation in single layer graphene and few layer graphene by first principles, *Nano Lett.*, 12 (9), 4624–4628.

[71] Barabanova, L., and Buldum, A., 2024, A first principles study of lithium adsorption in nanoporous graphene, *Nanomaterials*, 14 (18), 1528.